ACS SENSORS

pubs.acs.org/acssensors Article

Engineering Perovskite Hydroxide as a Cold-Adapted Oxidase Mimic for Construction of the Robust Low-Temperature Adaptive Biosensors

Yufeng Liu,[#] Jing Zhang,[#] Yuxin Wan,[#] Cong Li, Shuai Cui, Xuejiao J. Gao,* Hui Wei,* and Dongzhi Yang*

Cite This: *ACS Sens.* 2025, 10, 1844−1856 Read Online

ACCESS | Metrics & More | Article Recommendations | Supporting Information

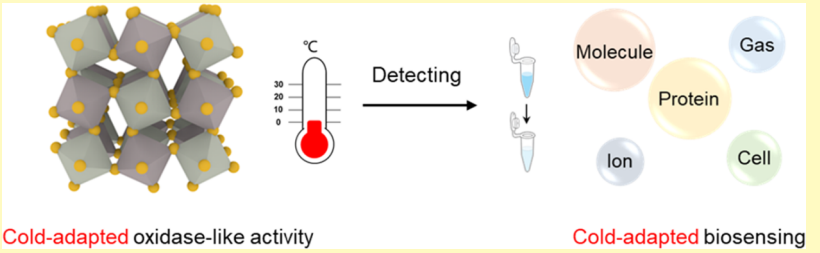

ABSTRACT: Traditional biological detection methods rely on signal amplification strategies such as enzymatic catalysis or nucleic acid amplification. However, their efficiency decreases in low-temperature environments, compromising their detection sensitivity. To break the loss of enzyme catalytic activity at low temperatures, research on cold-adaptive nanozymes has attracted much attention. Till now, only a few nanozymes have been reported to have cold-resistant catalytic properties. Here, a new type of cold-adapted nanozyme was constructed by engineering a perovskite hydroxide. The nanozyme not only boosted the oxidase-like catalytic activity by 2 orders of magnitude but also retained excellent catalytic performance at 0 °C. This enhanced activity may be attributed to the increase in manganese content, vacancy oxygen, and tetravalent manganese. Then, a robust low-temperature adaptive biosensor was established with a cold adaptive nanozyme. Notably, the detection of sulfide ion, ascorbic acid, alkaline phosphatase, and cellular glutathione by the cold-adapted probe was less affected by the temperature reduction, and the detection sensitivity of the probe for ALP at 0 °C is better than that of a commercial kit. Finally, the cold-adapted nanozyme was further used to construct a paper-based H_2S gas colorimetric probe. This study develops a new cold adaptive nanozyme and broadens the application scenarios of the nanozymes.

KEYWORDS: *cold-adaptive catalysis, nanozymes, perovskite hydroxide, biosensor, oxidase mimic*

In cold regions and areas requiring operation at low temperatures (e.g., cold chain transportation), it remains enormously challenging to reliably obtain bioanalysis results.[1,2] Most biological kits have an "optimal" detection temperature range. When the ambient temperature exceeds this, the accuracy of the results will be impacted. Traditional biological detection methods rely on biochemical reaction signal amplification (like enzymatic catalysis or nucleic acid amplification) for sensitivity.[3−6] However, low temperatures significantly diminish these reactions' efficiency, thus decreasing detection sensitivity. In addition, when ambient temperatures are low, the function of electronic sensors and detection equipment also will be heavily impacted.[7,8] Therefore, developing bioanalysis technologies adaptable to low-temperature environments and enhancing detection working capabilities and compatibility has a huge research importance and applicability potential.

As a biocatalyst with both high catalytic efficiency and strong substrate specificity, enzymes have been widely utilized in the field of analytical technologies.[9,10] They can not only considerably amplify the detection signal with outstanding catalytic efficiency but also effectively remove the interference of other substances in the detection process. However, most biological enzymes have an optimal catalytic temperature within a narrow physiological range.[11,12] As temperatures decrease, the enzyme's catalytic ability is greatly diminished.[13] Meanwhile, extracting, preparing, and utilizing enzymes also incur relatively high costs. Therefore, designing enzyme mimics that can preserve catalytic function at low-temperatures while proving inexpensive, and employing them in developing

Received: October 14, 2024
Revised: February 20, 2025
Accepted: March 3, 2025
Published: March 12, 2025

https://doi.org/10.1021/acssensors.4c02848
ACS Sens. 2025, 10, 1844−1856

Scheme 1. Schematic Illustration of the Preparation of Cold-Adapted Nanozymes Derived from Perovskite Hydroxide and Exploration of Their Biosensing Performance for Multiple Analytes at RT and 0 °C

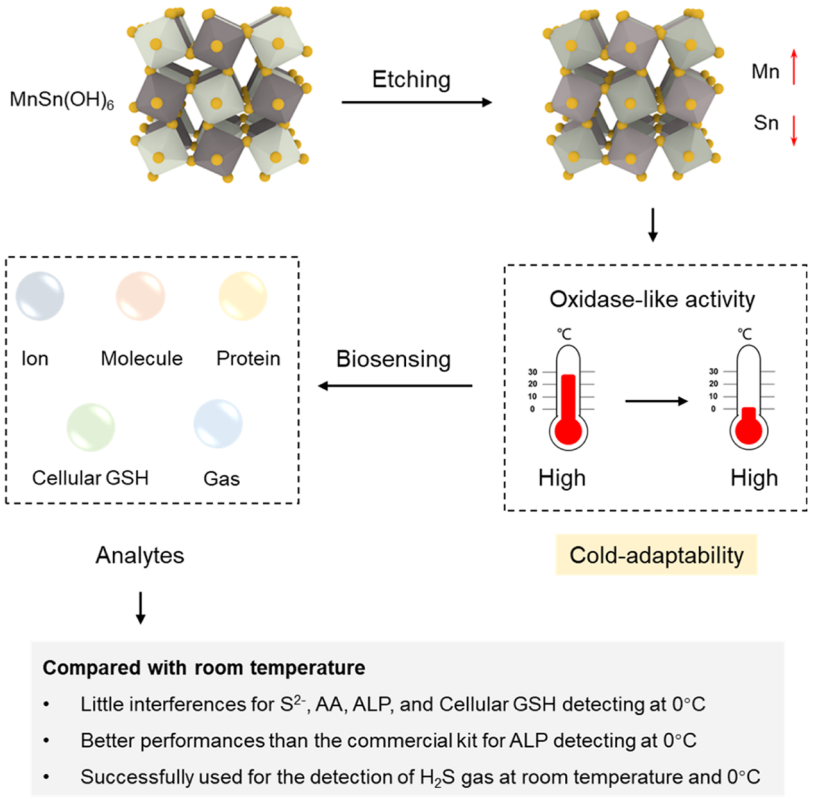

bioanalytical tools is anticipated to furnish novel low-temperature adaptive biosensors.[14−16]

Nanozymes refer to nanomaterials with enzyme-like catalytic properties.[17−19] Due to their diverse abilities and capacity for extensive manufacturing, nanozymes could serve as a hopeful category of enzyme alternatives.[20−27] Although the types and numbers of nanozymes discovered so far are substantial, the number of nanozymes with truly outstanding low-temperature catalytic proficiency remains quite limited. The research exploring cold-adaptive nanozymes is in its early stages, and the few existing examples so far have been based primarily on metal−organic frameworks (MOFs),[28,29] single-atom compositions,[30] metal oxides,[31] and magnetoelectric coupling materials.[32] Meanwhile, there are few reports on the use of cold-adaptive nanozymes to construct low-temperature resistant biosensors. To this end, it is urgent to create novel cold-adaptive catalytic nanozymes and systematically explore their low-temperature resistant biological detection performance.

In this work, as shown in Scheme 1, by engineering perovskite hydroxide, we obtained a novel cold-tolerant oxidase mimic. The catalytic efficiency of the engineered nanozyme in oxidase-like reactions could be increased by 2 orders of magnitude, and its catalytic function could still be sustained at over 90% in the temperature range from 37 to 0 °C. Through X-ray photoelectron spectroscopy (XPS), inductively coupled plasma mass spectrometry (ICP-MS), and Brunauer−Emmett−Teller (BET) measurements, we found that the enhanced activity stemmed primarily from elevated manganese content, vacancy oxygen, and tetravalent manganese. Later, we utilized this cold-adapted nanozyme to develop an innovative colorimetric probe and systematically evaluated its ability to detect ions, small molecules, and proteins at room temperature (RT) and 0 °C. The results revealed that probe sensitivity for sulfide ions, ascorbic acid, alkaline phosphatase (ALP), and cellular glutathione (GSH) at 0 °C approximated that at RT. Also, for ALP detection, its detecting sensitivity at 0 °C surpassed that of a commercially available kit. Finally, we used this nanozyme to assemble a novel gas colorimetric sensor on paper and successfully detected H_2S at RT and 0 °C, providing a new method for detecting the freshness of meat during subsequent low-temperature transportation.

MATERIALS AND EXPERIMENT

Materials and Characterizations. Cobalt nitrate hexahydrate ($Co(NO_3)_2·6H_2O$), magnesium nitrate hexahydrate ($Mg(NO_3)_2·6H_2O$), ferrous sulfate heptahydrate ($FeSO_4·7H_2O$), manganese acetate tetrahydrate ($(CH_3COO)_2Mn·4H_2O$), copper sulfate pentahydrate ($CuSO_4·5H_2O$), zinc nitrate hexahydrate ($Zn(NO_3)_2·6H_2O$), tetratin tetrachloride pentahydrate($SnCl_4·5H_2O$), sodium citrate ($C_6H_5Na_3O_7$), sodium hydroxide (NaOH), sodium sulfide(Na_2S), 3,3′,5,5′-tetramethylbenzidine (TMB), *p*-benzoquinone, poly(vinylpyrrolidone) (PVP), glutathione (GSH), and *N*,*N*-dimethylformamide (DMF) were purchased from Macklin. Chloroplatinic acid (H_2PtCl_6), sodium acetate, acetic acid, *β*-carotene, ascorbic acid (AA), and 2-Phospho-L-ascorbic acid trisodium acid (AAP) were purchased from Aladdin. ALP was purchased from Shanghai yuanye Bio-Technology Co., Ltd. Alkaline phosphatase assay kit was purchased from Beyotime Biotechnology. 30% hydrogen peroxide, acetone, chloroform, isopropanol, and *n*-hexane were purchased from Sinopharm Group. All materials were used as received. Deionized water was used to prepare all of the buffers and solutions.

UV−visible absorption spectra were recorded on a UV−visible spectrophotometer (UV 2600, Shimadzu, Japan). The absorption of a 96-well plate was recorded on a microplate reader (Bio Tek, Synergy H1). SEM images were recorded on a field emission electron scanning

https://doi.org/10.1021/acssensors.4c02848
ACS Sens. 2025, 10, 1844−1856

microscope (FEI Teneo VS) at an acceleration voltage of 20 kV. TEM-mapping images were recorded on a transmission electron microscope (SuperX Fei). PXRD patterns were recorded on an X-ray diffractometer (XRD) (Rigaku Miniflex 600, Japan). ICP-MS measurements were recorded on an inductively coupled plasma-mass spectrometer (Agilent 7700). XPS measurements were performed on an X-ray photoelectron spectrometer (Thermo Scientific K-Alpha). BET measurements were recorded on an automatic surface and porosity analyzer (Thermo Scientific K-Alpha).

Synthesis of $MnSn(OH)_6$. Perovskite hydroxides $MnSn(OH)_6$ was synthesized by coprecipitation method according to literature with some modifications.[33] Solution A: $CH_3(COO)_2Mn{\cdot}4H_2O$ (2 mmol) and sodium citrate (2 mmol) were dissolved in 70 mL of deionized water. Solution B: $SnCl_4{\cdot}5H_2O$ (2 mmol) was dissolved in 10 mL of ethanol. Solution B was mixed with solution A with 30 min of stirring. NaOH (10 mL, 2 M) was added to this mixed solution in a water bath under different temperatures (0, 23, 54, 80, and 100 °C). After 1 h, the precipitate was collected by centrifugation, washed several times with ethanol and deionized water, and dried at 60 °C. The perovskite hydroxides prepared at 0, 23, 54, and 100 °C were denoted as $MnSn(OH)_{6-0}$, $MnSn(OH)_{6-23}$, $MnSn(OH)_{6-54}$ and $MnSn(OH)_{6-100}$. $CoSn(OH)_6$, $MgSn(OH)_6$, $FeSn(OH)_6$, $CuSn(OH)_6$, and $ZnSn(OH)_6$ were synthesized using the same procedures described above except that the metal in solution A is different.

Synthesis of $MnSn(OH)_{6-23-E10}$. The synthesis of $MnSn(OH)_{6-23-E10}$ referred to a previous report.[34] $MnSn(OH)_{6-23}$ (30 mg) was dispersed in 9 mL of distilled water, and then NaOH (4 mL, 8 M) was added and stirred at RT for 10 min. The residual powder was collected by centrifugation after repeated washing with distilled water and ethanol, and finally dried at 60 °C.

Synthesis of Pt NPs. Pt NPs were synthesized by following a previous procedure with minor modifications.[35] PVP (133 mg, MW = 40,000) was dissolved in methanol (45 mL), and then H_2PtCl_6 (5 mL, 50 mM) was added to the solution. The mixture was refluxed for 3 h at 70 °C. After that, methanol was removed by using a rotary evaporator, and then the NPs were precipitated by acetone for 3 h and collected by centrifugation (6000 rpm, 3 min). The obtained Pt NPs were further purified with chloroform and hexane and then redispersed in DMF.

Oxidase-like Activity Assay. TMB (500 μM) and nanozyme (0.01 mg/mL) were incubated in a phosphate buffer (pH 4.5) for 5 min. Subsequently, the reaction solution was transferred to a 96-well plate, and the absorbance value at 652 nm was measured using a microplate reader. It is worth noting that when comparing the oxidase-like activity of different metals and different water bath temperatures, the concentration of the nanozyme was 0.1 mg/mL.

Peroxide-like Activity Assay. TMB (500 μM), H_2O_2 (500 μM), and nanozymes (0.01 mg/mL) were incubated in a phosphate buffer (pH 4.5) for 5 min. Subsequently, the reaction solution was transferred to a 96-well plate and the absorbance value at 652 nm was measured using a microplate reader.

Catalase-like Activity Assay. H_2O_2 (500 μM) and nanozyme (0.01 mg/mL) were mixed in phosphate-buffered saline (PBS buffer) (pH 7.0), and the absorbance change at 240 nm was measured within 1 min using a UV−visible spectrophotometer.

Kinetics Assays. Various concentrations of TMB were reacted with 0.01 mg/mL nanozymes and phosphate buffer (pH 4.5) at RT for 5 min, respectively. Michaelis−Menten equation ($V = V_{max}[S]/(K_m + [S])$) was applied to obtain the kinetic parameters V_{max} and K_m. $k_{cat} = V_{max}/[E]$. $[E]$ is the enzyme or nanozyme concentration. The molar concentration of the nanozyme was determined by a nanoparticle tracking analysis (NTA) system. First, measure the number of particles per milliliter with the NTA Instruments and then divide it by Avogadro's constant to get $[E]$. All measurements were replicated at least three times and averaged for the sake of accuracy.

Reaction with TMB in the Presence of Various Radical Scavengers. Various radical scavengers (*p*-benzoquinone, *β*-carotene, and isopropanol) were reacted with nanozyme (0.01 mg/mL) and TMB (500 μM) in phosphate buffer (pH 4.5) at RT for 5 min, respectively. Then, the reaction solution was transferred to a 96-well plate, and data collection was performed by measuring the absorbance value at 652 nm using a microplate reader.

Measurements of Mn and Sn Contents. The amounts of Mn and Sn in $MnSn(OH)_{6-23}$ and $MnSn(OH)_{6-23-E10}$ were analyzed by ICP-MS (Agilent 7700). Before the measurement, $MnSn(OH)_{6-23}$ and $MnSn(OH)_{6-23-E10}$ were digested with aqua regia, respectively.

Detection of S^{2-}. RT: Different concentrations of Na_2S (0, 1, 2, 3, 4, 5, 10, 20, 40, 60, 80, and 100 μM) were reacted with nanozyme (0.01 mg/mL) and TMB (500 μM) in phosphate buffer (pH 4.5) at RT for 5 min, respectively. Different concentrations of Na_2S (0, 1, 2, 3, 4, 5, 10, 20, 40, 60, 80, and 100 μM) were reacted with nanozyme (0.01 mg/mL) and TMB (500 μM) in phosphate buffer (pH 4.5) at 0 °C for 5 min, respectively. The detection limit was calculated by $3\sigma/b$, where σ is the standard deviation of the blank signal, and b is the slope of the regression line.

Detecting Selectivity of S^{2-}. Different ions (0.5 mg/mL) were reacted with nanozyme (0.01 mg/mL) and TMB (500 μM) in phosphate buffer (pH 4.5) at RT for 5 min, respectively. The absorbance at 652 nm was collected by using a microplate reader.

Detection of AA. RT: Different concentrations of AA (0, 1, 2, 3, 4, 5, 6, 7, 8, 9, 10, 15, 20, 30, and 50 μM) were reacted with nanozyme (0.01 mg/mL) and TMB (500 μM) in phosphate buffer (pH 4.5) at RT for 5 min, respectively. Different concentrations of AA (0, 1, 2, 3, 4, 5, 6, 7, 8, 9,10, 15, 20, 30, and 50 μM) were reacted with nanozyme (0.01 mg/mL) and TMB (500 μM) in phosphate buffer (pH 4.5) at 0 °C for 5 min, respectively. The detection limit was calculated by $3\sigma/b$, where σ is the standard deviation of the blank signals and b is the slope of the regression line.

Detecting Selectivity of AA. Different small biological molecules (0.5 mg/mL) were reacted with nanozyme (0.01 mg/mL) and TMB (500 μM) in phosphate buffer (pH 4.5) at RT for 5 min, respectively. The absorbance at 652 nm was collected using a microplate reader.

Detection of ALP. RT: Different concentrations of ALP (0, 0.5, 1, 2, 4, 6, 8, and 10 U L^{-1}) and AAP (2 mM) were first added to PBS buffer (pH 8.0) at RT for 30 min, respectively. Subsequently, nanozyme (0.01 mg/mL), phosphate buffer (pH 4.5), and TMB (500 μM) were added to the mixture, which was further incubated at RT for 5 min before measurements. Different concentrations of ALP (0, 0.5, 1, 2, 4, 6, 8, and 10 U L^{-1}) and AAP (2 mM) were first added to PBS buffer (pH 8.0) at 0 °C for 30 min, respectively. Subsequently, nanozyme (0.01 mg/mL), phosphate buffer (pH 4.5), and TMB (500 μM) were added to the mixture, which was further incubated at 0 °C for 5 min before measurements. The detection limit was calculated by $3\sigma/b$, where σ is the standard deviation of the blank signals, and b is the slope of the regression line.

Detection of ALP via ALP Assay Kits. According to the protocol of the ALP assay kits. Different concentrations of ALP (1 μL) were first incubated with chromogenic substrate solution (50 μL) in their assay buffer (49 μL) for 30 min, respectively. Then, the reaction stop solution (100 μL) was added. The absorbance at 405 nm was measured by using a microplate reader. The detection limit was calculated by $3\sigma/b$, where σ is the standard deviation of the blank signals, and b is the slope of the regression line.

Detecting Selectivity of ALP. Different analytes (20 U L^{-1}: ALP, glucose oxidase (GOX), acetylcholinesterase (AChE); 200 mM: glutamic acid (Glu), alanine (Ala), valine (Val); 0.1 mg/mL: bovine serum albumin (BSA), Na^+, K^+, Ca^{2+}) were reacted with AAP (2 mM) and PBS buffer (pH 8.0) at 37 °C for 30 min, respectively. Subsequently, nanozyme (0.01 mg/mL), phosphate buffer (pH 4.5), and TMB (500 μM) were added to the mixture, and the mixture was incubated at RT for 5 min. The absorbance at 652 nm was collected using a microplate reader.

Nanozyme-Based Paper Sensor for Detecting H_2S Gas (Produced during Chemical Reactions) at RT and 0 °C. The preparation of paper-based colorimetric interface referred to a previous report.[36] H_2S gas was generated by adding Na_2S into HCl solution.[37] The first step is to divide the filter paper into multiple 2 cm × 2 cm areas; the second step is to drop 10 μL of a 1 mg/mL nanozyme solution in the center of each area and let it air-dry at RT; the third step is to place the treated filter paper and a brown glass

https://doi.org/10.1021/acssensors.4c02848
ACS Sens. 2025, 10, 1844−1856

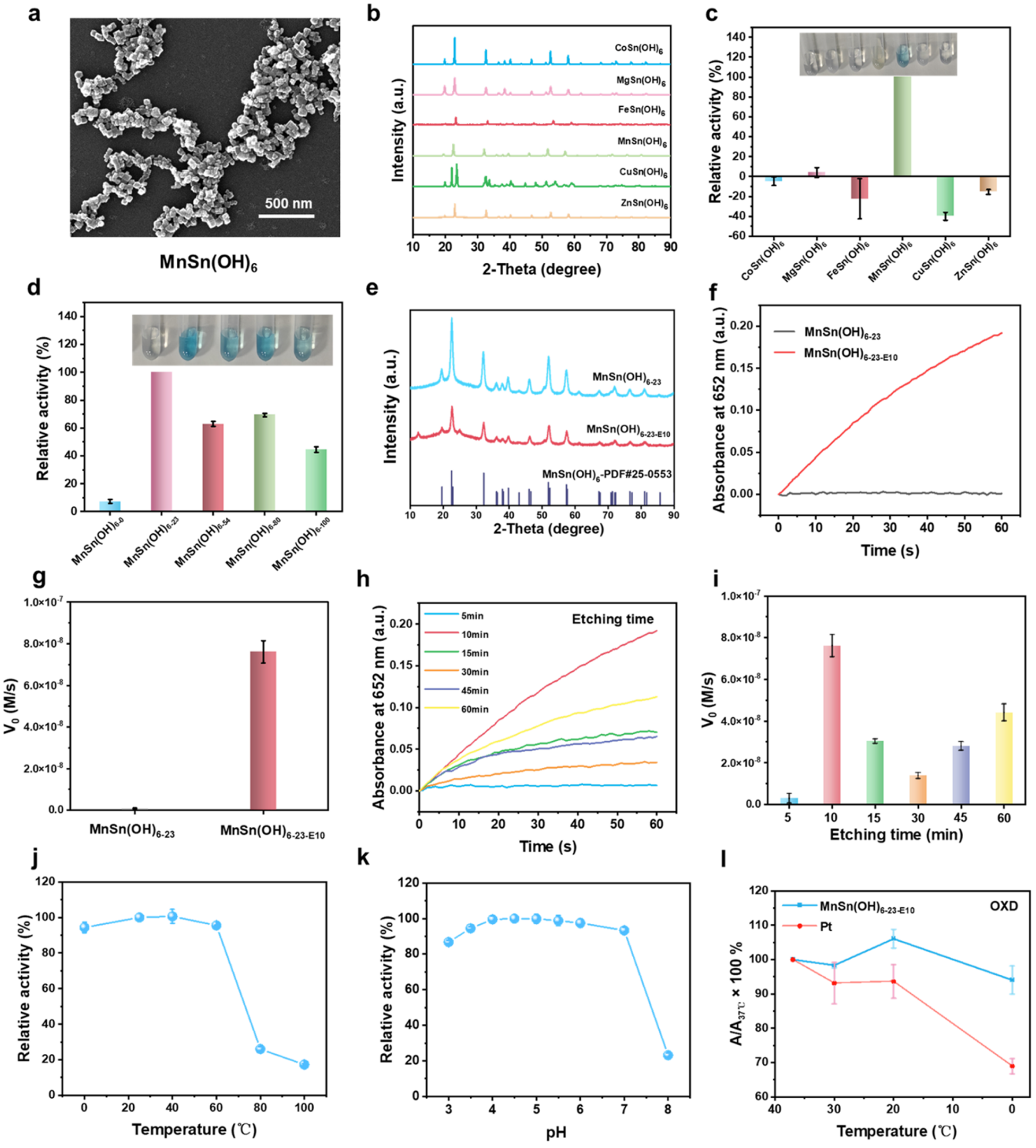

Figure 1. (a) SEM image of $MnSn(OH)_6$. (b) PXRD patterns of $CoSn(OH)_6$, $MgSn(OH)_6$, $FeSn(OH)_6$, $MnSn(OH)_6$, $CuSn(OH)_6$, and $ZnSn(OH)_6$. (c) Relative oxidase-like activity of six perovskite hydroxides; the oxidase-like activity of $MnSn(OH)_6$ was set as 100%. Inset: Photograph of the corresponding samples. (d) Relative oxidase-like activity of five perovskite hydroxides with different synthetic temperatures; the oxidase-like activity of $MnSn(OH)_{6-23}$ was set as 100%. Inset: Photograph of the corresponding samples. (e) PXRD patterns of $MnSn(OH)_{6-23}$ and $MnSn(OH)_{6-23\text{-}E10}$. The line at the bottom marks the reference pattern of $MnSn(OH)_6$ from the JCPDS database. (f) Time evolution of the absorbance at 652 nm for monitoring the oxidase-mimicking catalytic activities of $MnSn(OH)_{6-23}$ and $MnSn(OH)_{6-23\text{-}E10}$. (g) Initial velocities (V_0) corresponding to panel (f). (h) Time evolution of absorbance at 652 nm for monitoring the oxidase-mimicking catalytic activities of $MnSn(OH)_{6-23}$ under different etching time. (i) V_0 corresponding to panel h. Relative oxidase-like activity of $MnSn(OH)_{6-23\text{-}E10}$ under different (j) temperatures and (k) pH. (l) Normalized catalytic activity ($A/A_{37\ °C}$, $A_{37\ °C}$: the absorbance of 652 nm at 37 °C) of $MnSn(OH)_{6-23\text{-}E10}$ and Pt NPs at varied temperatures. Error bars in all figures are mean standard deviations of 3 independent tests.

https://doi.org/10.1021/acssensors.4c02848
ACS Sens. 2025, 10, 1844−1856

bottle containing various concentrations of Na_2S and HCl in a sealed plastic bag and react at RT for 1 h. The fourth step is to remove the filter paper after reaction and spot the center area with 25 mM TMB for reaction. The fifth step is to use a smartphone (Xiaomi 11) to photograph the reacted filter paper, then use Photoshop to extract RGB (RGB, short for "Red, Green, and Blue") values from the image for quantitative analysis. When repeating at 0 °C, the prepared reagents should be precooled in the refrigerator at 0 °C in advance, and the entire reaction should be carried out in the refrigerator at 0 °C.

Nanozyme-Based Paper Sensor for Detecting H_2S Gas (Produced during Meat Spoilage) at RT and 0 °C. The pork was divided into 5, 10, 20, 30, and 50 g portions, sealed in a plastic bag, and left at RT for 18 h. Then, the paper-based sensor with nanozymes was placed in the bag and incubated at RT and 0 °C for 1 h. Afterward, the sensor was removed and 10 μL of 25 mM TMB was added to its center. Finally, a photograph was taken with a mobile phone, and the RGB value was extracted and analyzed using Photoshop.

Detecting of GSH. RT: Different concentrations of GSH (0, 1, 2, 4, 6, 8, 10, 20, 40, and 60 μM) were reacted with nanozyme (0.01 mg/mL) and TMB (500 μM) in phosphate buffer (pH 4.5) at RT for 5 min, respectively. Different concentrations of GSH (0, 1, 2, 4, 6, 8, 10, 20, 40, and 60 μM) were reacted with nanozyme (0.01 mg/mL) and TMB (500 μM) in phosphate buffer (pH 4.5) at 0 °C for 5 min, respectively. The detection limit was calculated by $3\sigma/b$, where σ is the standard deviation of the blank signal and b is the slope of the regression line.

Cell Culture and Lysate Preparation. Cells were cultured in high-glucose Dulbecco's modified Eagle's medium (DMEM) supplemented with 10% FBS under an atmosphere of 5% CO_2 at 37 °C. When the cell density reached 80%, the L929 and 4T1 cells were collected and washed with chilled phosphate-buffered saline (PBS). Then, according to the amount of ground cells in the EP tube, an equal volume of cell lysate was added (lysate/PMSF/phosphatase inhibitor = 100:1:1), and the iceberg broke for 40 min, with a vortex every 10 min. Finally, the sample was centrifuged at 4 °C for 20 min at 12,000 rpm. The supernatants were transferred to the tubes for the following detection assays: nanozyme (0.01 mg/mL), TMB (500 μM), and different amounts of L929 and 4T1 lysate in phosphate buffer (pH 4.5) at RT or 0 °C for 5 min. After centrifugation at 12,000 rpm for 2 min, the absorbance at 652 nm was collected on a microplate reader.

Theoretical Calculation. Geometry optimizations and energy calculations were conducted by using the generalized gradient approximation (GGA) with the Perdew–Burke–Ernzerhof functional, incorporating van der Waals corrections within the DFT-D3BJ framework. A high energy cutoff of 500 eV was employed, alongside Gaussian smearing with a width of 0.05 eV to ensure enhanced computational accuracy. To account for the significant on-site Coulomb interactions associated with the localized d electrons in Mn, the Hubbard U correction was applied, with an effective U (U_{eff}) value of 3.0 eV. The Brillouin zone integrations were meticulously carried out using (3 × 3 × 1) Monkhorst–Pack k-point meshes. Convergence criteria were stringently set at 10^{-5} eV for the electronic structure and 0.02 eV $Å^{-1}$ for ionic forces to ensure precision in the calculations. These simulations were performed using the Vienna Ab initio Simulation Package (VASP) and employed the projector-augmented wave method for the pseudopotentials.

RESULTS AND DISCUSSION

Engineering Perovskite Hydroxide with Cold-Adapted Oxidase-like Activity. Here, six perovskite hydroxides ($MSn(OH)_6$, M = Co, Mg, Fe, Mn, Cu, and Zn) were synthesized using a simple coprecipitation method.[38] As shown in Figures 1a and S1, scanning electron microscopy (SEM) showed the cubic morphology with various sizes ranging from 10 to 600 nm. The powder X-ray diffraction (PXRD) spectra in Figure 1b confirms that all of these perovskite hydroxides match with a previous report,[39] further validating their successful synthesis. To evaluate the oxidase-mimicking activity of these perovskite hydroxides, UV–visible spectroscopy was applied to monitor the catalytic oxidation of the typical oxidase chromogenic substrate 3,3′,5,5′-tetramethylbenzidine (TMB). As shown in Figures 1c and S2, removing the background absorption interference of the material itself, only $MnSn(OH)_6$ catalyzed the oxidation of TMB and produced a blue color. The oxidized TMB showed an obvious UV–visible absorption peak at 652 nm, demonstrating the oxidase-mimicking activity of $MnSn(OH)_6$. In contrast, TMB mixed with the other five perovskite hydroxides produced neither colored products nor characteristic absorptions, which indicated that the Mn element was critical for the oxidase-like activity of the perovskite hydroxide.

To engineer the oxidase-like activity of $MnSn(OH)_6$, we optimized the synthesis methods of $MnSn(OH)_6$. As shown in Figures S3 and S4, $MnSn(OH)_6$ has been successfully synthesized at 0, 23, 54, 80, and 100 °C, respectively. (The subscript of the chemical formula indicates the temperature at which the synthesis was performed.) Among them, the $MnSn(OH)_{6-23}$ synthesize at 23 °C exhibited the highest oxidase-mimicking activity (Figures 1d and S5). Although the synthetic temperatures affected the potential of perovskite hydroxides (Figure S6), there seems to be no significant correlation between the potentials and their oxidase-like activities. Besides, we further optimized the material's oxidase-like activity by etching.[34] As shown in Figures 1e and S7a, $MnSn(OH)_{6-23-E10}$ can still maintain its crystal structure after being etched with sodium hydroxide for 10 min (subscript E10 means etching for 10 min). Surprisingly, after being etched for only 10 min, the oxidase-like catalytic activity of $MnSn(OH)_{6-23-E10}$ increased over 100 times compared to its original rate (Figure 1f,g). Encouraged by this, we further screened the etching time, and the optimized etching time of $MnSn(OH)_{6-23}$ was 10 min (Figure 1h,i). Such an optimal etching time can be ascribed to $MnSn(OH)_{6-23-E10}$ possessing the greatest negative charge (Figure S7b), allowing it to elevate its attraction for TMB (which carries a positive charge) through electrostatic engagement. To explore whether $MnSn(OH)_{6-23-E10}$ has other enzymatic activities besides OXD, we compared the peroxidase (POD)-like activity of $MnSn(OH)_{6-23}$ before and after etching. As shown in Figure S10c,d, there was almost no POD-like activity of $MnSn(OH)_{6-23}$ before and after engineering.

To evaluate the cold-adapted enzyme-like activity of $MnSn(OH)_{6-23-E10}$, the oxidase-like activity of $MnSn(OH)_{6-23-E10}$ at 25 °C was set as 100% and the activity changes were compared at temperatures of 0, 40, 60, 80, and 100 °C. Figures 1j and S8a showed that $MnSn(OH)_{6-23-E10}$ can maintain its excellent catalytic performance in the range of 0–60 °C, but its activities decrease significantly when the temperature rises to 80 and 100 °C. In addition, $MnSn(OH)_{6-23-E10}$ has a wide pH adaptability range and can maintain its oxidase-like activity in the pH values from 3.5 to 7 (Figures 1k and S8b). Subsequently, we synthesized the Pt nanozyme, known for strong oxidase-like activity, and evaluated its cold-adapted catalytic performance compared to ours (Figure S9). As shown in Figures 1l and S10b, the activity of Pt nanozyme was lost by more than 30% when the temperature dropped from 37 to 0 °C, while that of $MnSn(OH)_{6-23-E10}$ nanozyme was only lost by about 5%. Apart from the Pt nanozyme, the oxidase-like activity of CeO_2

https://doi.org/10.1021/acssensors.4c02848
ACS Sens. 2025, 10, 1844–1856

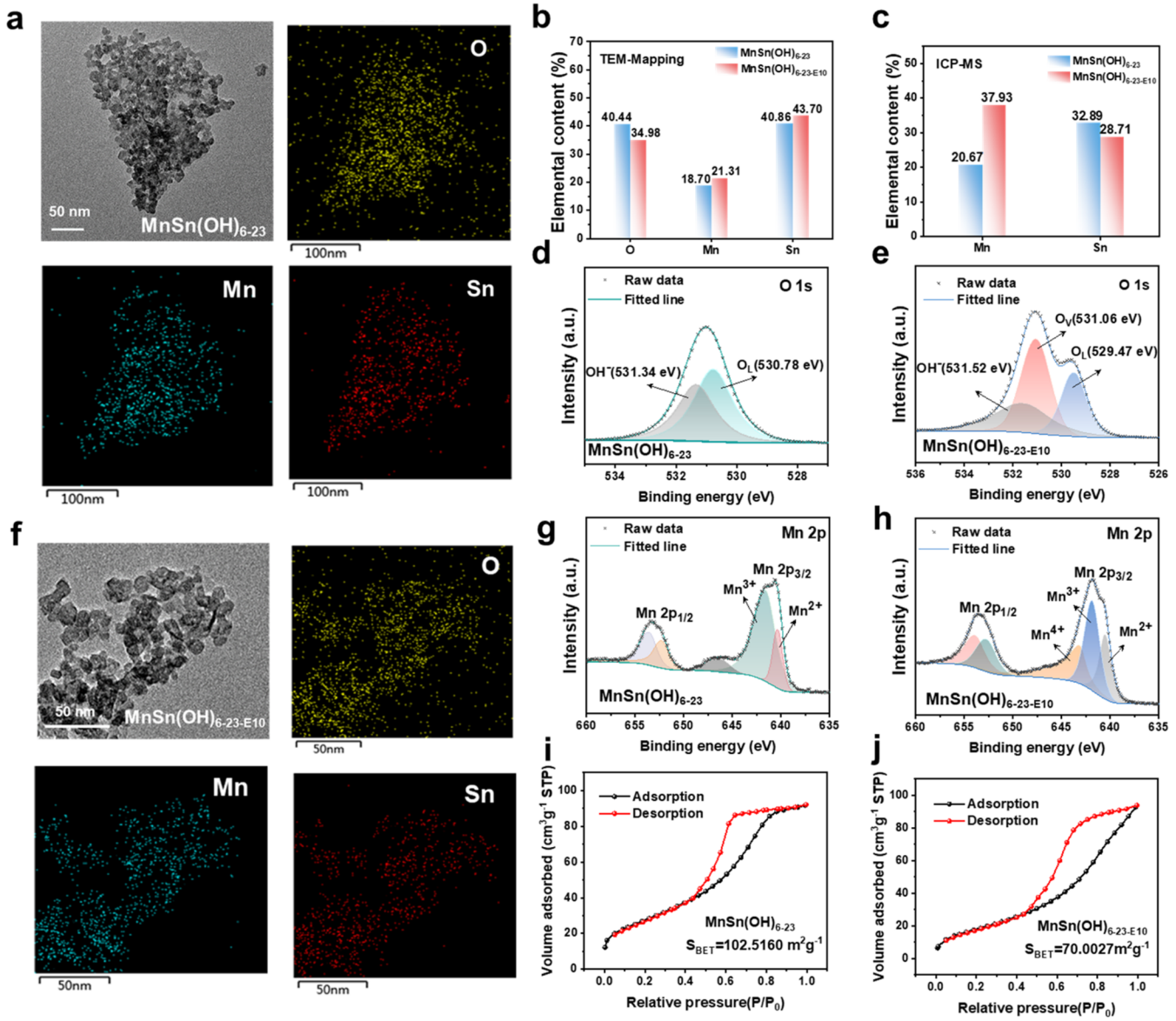

Figure 2. (a) TEM and EDS elemental mapping images of $MnSn(OH)_{6-23}$. (b) Elemental content of O, Mn, and Sn corresponding to panels (a) and (f). (c) Elemental content of Mn and Sn in $MnSn(OH)_{6-23}$ and $MnSn(OH)_{6-23-E10}$ under ICP-MS measurements. The O 1s XPS spectra of (d) $MnSn(OH)_{6-23}$ and (e) $MnSn(OH)_{6-23-E10}$. (f) TEM and EDS elemental mapping images of $MnSn(OH)_{6-23-E10}$. The Mn 2p XPS spectra of (g) $MnSn(OH)_{6-23}$ and (h) $MnSn(OH)_{6-23-E10}$. The BET surface area measurements of (i) $MnSn(OH)_{6-23}$ and (j) $MnSn(OH)_{6-23-E10}$.

nanozyme also decreases significantly at 0 °C (Figure S11). These findings further demonstrate the unique advantage of our nanozymes in low-temperature catalytic performance.

Mechanism Study. To explore the reactive oxygen species (ROS) during the oxidase-like catalytic reaction, *p*-benzoquinone, *β*-carotene, and isopropanol were selected for eliminating the possible involved superoxide anion, singlet oxygen, and hydroxyl radical.[28,40] The results suggested that the superoxide anion could be the main ROS catalyzed by the $MnSn(OH)_{6-23-E10}$ (Figure S10a). Then, TEM element mapping, ICP-MS, XPS, and BET measurements were used to analyze the differences in materials before and after etching. TEM mapping showed that elements of O, Mn, and Sn all exist before and after etching, but their contents have changed; that is, the content of O decreases and the contents of Mn and Sn increase (Figure 2a,b,f). In addition, the results of ICP-MS showed that after etching, the content of Mn increased from 20.67 to 37.93%, while the content of Sn decreased from 32.89 to 28.71%, which is consistent with previous research results that the contents of O and Sn will decrease after etching[34] (Figure 2c).

Meanwhile, an XPS analysis was applied to evaluate the changes in the valence state of elements before and after etching. The O 1s spectra in Figure 2d,e revealed that the perovskite hydroxide structure before etching contained lattice oxygen (O_L) and hydroxyl ions (OH^-). After etching, in addition to O_L and OH^-, vacancy oxygen (O_V) was generated. These newly produced O_V may also be the key factor in the enhanced catalytic activity of $MnSn(OH)_{6-23-E10}$. The spectra of Mn 2p showed that the high-valence Mn^{4+} is identified in $MnSn(OH)_{6-23-E10}$ after etching, which is consistent with a previous report that the high-valence Mn−O bonds are the active sites for the nanozyme to exhibit excellent oxidase-like activity at low-temperature[28] (Figure 2g,h).

https://doi.org/10.1021/acssensors.4c02848
ACS Sens. 2025, 10, 1844−1856

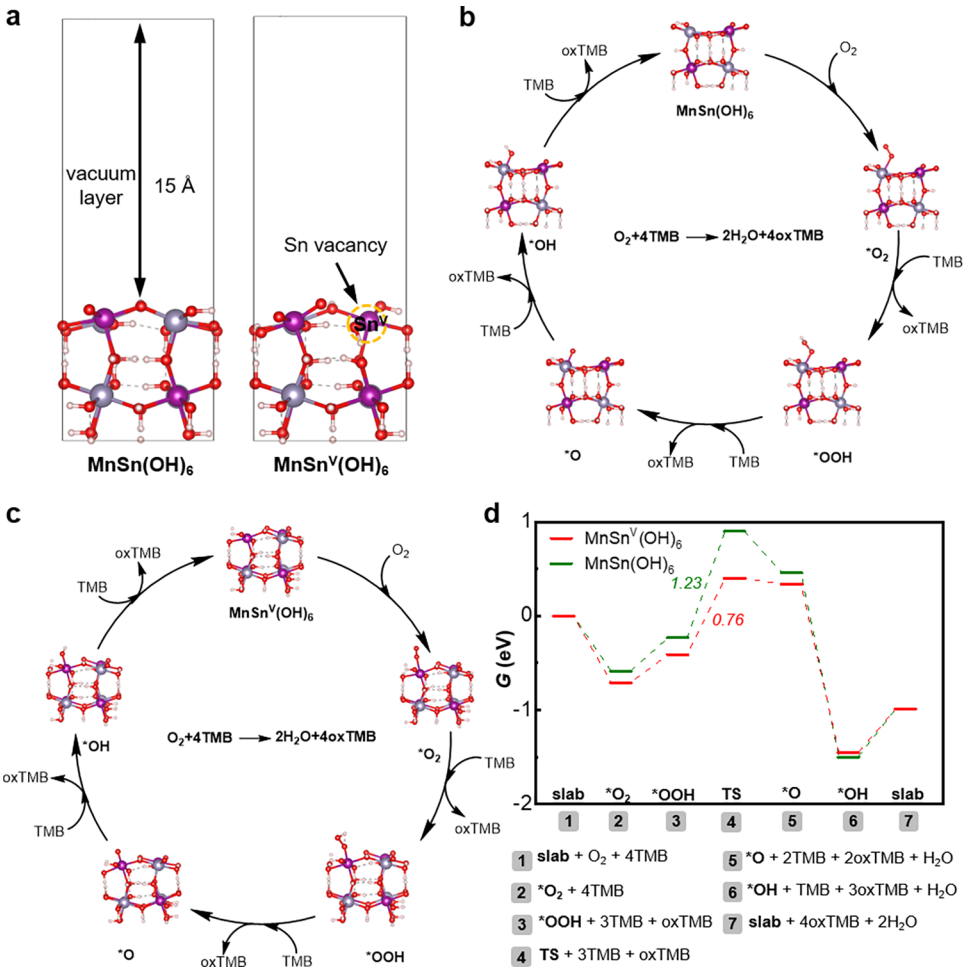

Figure 3. (a) The slab models with exposed (100) surfaces simulating the pre-etching ($MnSn(OH)_6$) and postetching ($MnSn^V(OH)_6$) with Sn vacancies.The vacuum layer thickness is set to 15 Å. Proposed reaction pathways for the reduction of O_2 to H_2O with optimal adsorption configurations on (b) $MnSn(OH)_6$ and (c) $MnSn^V(OH)_6$. (d) Energy profile diagram for the oxygen reduction reaction on $MnSn(OH)_6$ and $MnSn^V(OH)_6$ using TMB as the reducing agent.

Considering the importance of specific surface area to catalytic activity, we measured the BET surface areas of $MnSn(OH)_{6-23}$ and $MnSn(OH)_{6-23\text{-}E10}$. As shown in Figure 2i,j, the BET surface areas decreased from 102 to 70 $m^2\ g^{-1}$ after etching, indicating that the specific surface area is not the factor that improves its activity.

Density Functional Theory (DFT) calculations were employed to investigate the oxidase-like activity of the material surface in catalyzing O_2 activation of the substrate TMB before and after etching. Figure 3a illustrates the slab structure models of defect-free $MnSn(OH)_6$ with a (100) surface and $MnSn^V(OH)_6$ containing Sn vacancies, representing the material surface before and after etching, respectively. Figure 3b,c depicts the reaction pathways for O_2 activation of TMB catalyzed by $MnSn(OH)_6$ and $MnSn^V(OH)_6$, respectively, revealing a consistent catalytic mechanism. The process consists of five key steps. The first step is the O_2 adsorption on the surface Mn site, forming O_2* (* denotes the adsorption state). Secondly, O_2* abstracts a reducing H atom from TMB, generating *OOH; The *OOH species undergoes O−O bond cleavage via a transition state (TS), yielding *O and OH radicals. Concurrently, the OH radical abstracts a second H atom from another TMB molecule, forming H_2O. Subsequently, *O sequentially abstracts two more H atoms from additional TMB molecules, generating another H_2O molecule. Figure 3d presents the Gibbs free energy (G, in eV) profile for the reaction pathway. The potential energy surface analysis indicates that O−O bond cleavage in *OOH is the rate-determining step. The energy barrier for *OOH activation on $MnSn(OH)_6$ is 1.23 eV, whereas it significantly decreases to 0.76 eV for the etched $MnSn^V(OH)_6$, demonstrating the enhanced oxidase activity of the etched material. Furthermore, based on the thermodynamic relationship $G = U - \Delta TS$, under low entropy conditions (S = 44.320 J/(mol·K)), the activation energy barrier at 273.15 K is only 0.78 eV. This explains why $MnSn^V(OH)_6$ maintains high catalytic efficiency even at low temperatures, confirming its cold-adaptive catalytic capability.

Kinetic Study. The standard Michaelis−Menten curves were observed, and the kinetic parameters were derived using the equation: $V = V_{max}[S]/(K_m + [S])$, where V is the initial velocity, $[S]$ represents the concentration of substrate, V_{max} indicates the maximum reaction velocity, and the Michaelis constant K_m is the substrate concentration at which the reaction occurs at half of V_{max}. As shown in Figure S13 and Table S1, the catalytic efficiency (k_{cat}/K_m = 3.3 $mM^{-1}\ s^{-1}$) and the maximum reaction velocity ($V_{max} = 3.4 \times 10^{-11}$ mM s^{-1}) of etched $MnSn(OH)_{6-23\text{-}E10}$ are 2 orders of magnitude higher

https://doi.org/10.1021/acssensors.4c02848
ACS Sens. 2025, 10, 1844−1856

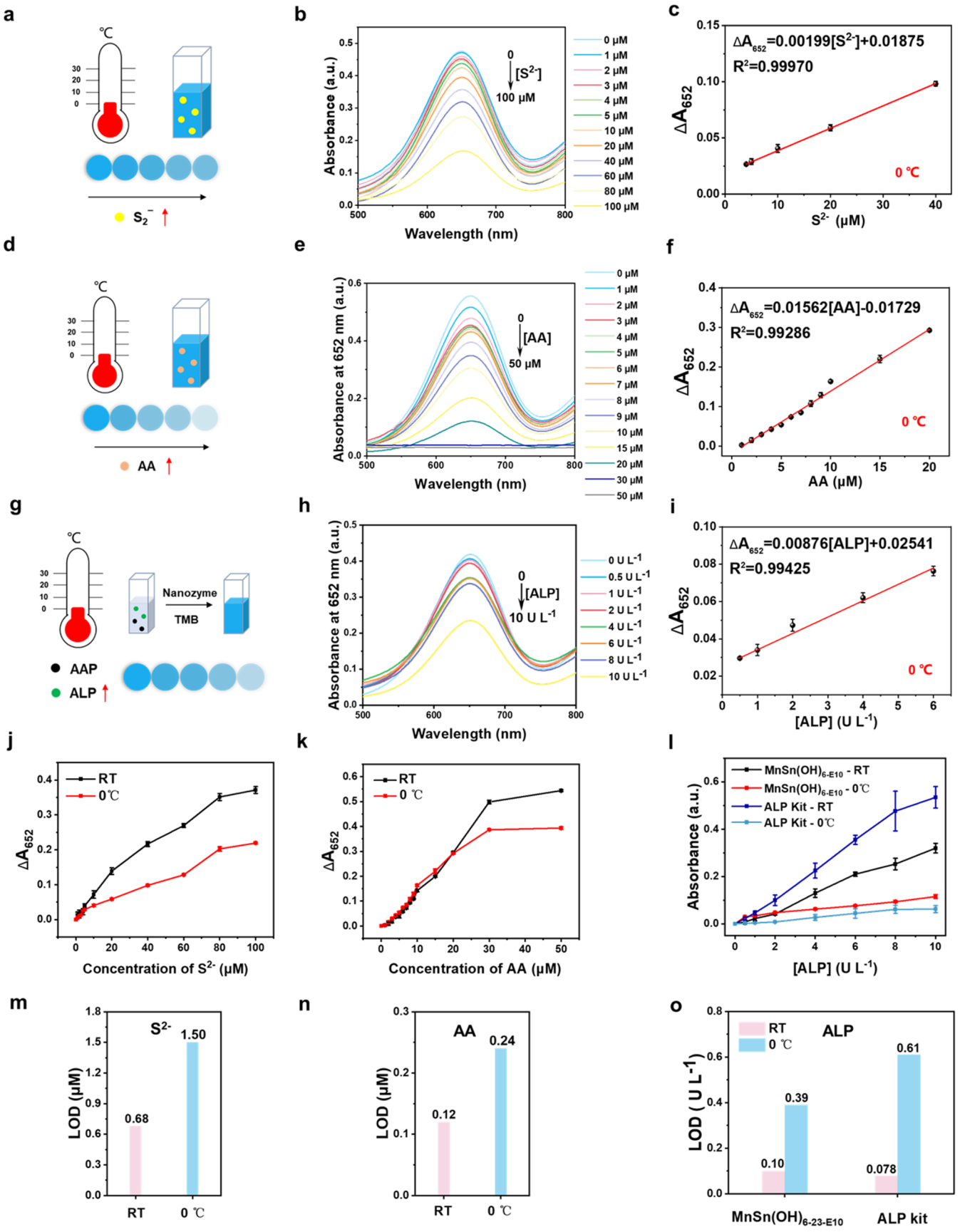

Figure 4. (a) Schematic diagram of the nanozyme probe detecting S^{2-} at 0 °C. (b) UV−visible absorption spectra of samples containing TMB and $MnSn(OH)_{6-23-E10}$ in the absence and presence of S^{2-} with different concentrations at 0 °C. (c) Linear calibration plotted in the concentration range from 4 to 40 μM at 0 °C. (d) Schematic diagram of the nanozyme probe detecting AA at 0 °C. (e) UV−visible absorption spectra of samples containing TMB and $MnSn(OH)_{6-23-E10}$ in the absence and presence of AA with different concentrations at 0 °C. (f) Linear calibration plotted in

https://doi.org/10.1021/acssensors.4c02848
ACS Sens. 2025, 10, 1844−1856

Figure 4. continued

the concentration range from 1 to 20 μM at 0 °C. (g) Schematic illustration of detecting ALP with $MnSn(OH)_{6-23-E10}$ at 0 °C. (h) UV−visible absorption spectra of samples containing TMB, AAP and $MnSn(OH)_{6-23-E10}$ in the absence and presence of ALP with different concentrations at 0 °C. (i) Linear calibration plotted in the concentration range of $MnSn(OH)_{6-23-E10}$ at 0 °C. Comparison of the sensitivity of the nanozyme probe for (j) S^{2-} and (k) AA detection at RT and 0 °C. (l) Comparison of the sensitivity of detecting ALP with the $MnSn(OH)_{6-23-E10}$ and ALP kit at RT or 0 °C. Detection limit of $MnSn(OH)_{6-23-E10}$ for (m) S^{2-} and (n) AA at RT and 0 °C. (o) Detection limit of $MnSn(OH)_{6-23-E10}$ and ALP kit for ALP at RT and 0 °C. Error bars in all figures mean standard deviations of 3 independent tests.

than that of $MnSn(OH)_{6-23}$ (k_{cat}/K_m = 7.2 × 10^{-3} mM^{-1} s^{-1}, V_{max} = 6.5 × 10^{-13} mM s^{-1}).

Low-Temperature Adaptive Detection of Ions, Small Molecules, and Proteins. Benefiting from the excellent cold-adaptive property of the engineered nanozyme, we constructed a low-temperature adaptive biosensor and systematically assessed its ability to detect ions, small molecules, and proteins at RT and 0 °C.

For ion detection, S^{2-} was chosen as the model due to its reducing property. As shown in Figure S16a,b, the $MnSn(OH)_{6-23-E10}$-based biosensor showed an excellent detectability toward S^{2-} at RT. Its linear relationship was in the range from 1 to 20 μM (Figure S16c) and the detection limit was 0.68 μM (Figure 4m and Table S3). In addition, the selectivity of this sensor was evaluated in a variety of common biological interfering ions, including Zn^{2+}, Mg^{2+}, Co^{2+}, Fe^{3+}, Na^{+}, La^{3+}, Lu^{3+}, Ce^{3+}, Hg^{2+}, Cu^{2+}, Ag^{+}, Cu^{+}, Ni^{2+}, Mn^{2+}, Cd^{2+}, Pd^{2+}, Ca^{2+}, Cr^{2+}, and NH^{4+}. The results showed that these ions had negligible interference in the detection of S^{2-} (Figure S17). Subsequently, we employed an identical sensor to detect S^{2-} at 0 °C (Figure 4a,b). Although the decrease in temperature causes a certain decrease in the sensitivity of detection, the probe still demonstrates an excellent S^{2-} detection performance at 0 °C, with a linear detection range of 4−40 μM and a limit of detection of 1.50 μM (Figure 4c,j,m and Table S3).

For small molecule detection, ascorbic acid (AA) with a reducing efficacy was analyzed. Figure S16d,e showed the excellent detectability of this probe toward AA at RT, with a linear detection range of 1−30 μM (Figure S16f) and a limit of detection of 0.12 μM (Figure 4n and Table S4). Similar to ion detection, we further explored the interference of temperature reduction on AA detection. Compared with the test results at RT, the cold-adapted biosensor exhibited high sensitivity in detecting AA within a linear range of 1−20 μM at 0 °C, with a detection limit of 0.24 μM (Figure 4d,e,f,k,n and Table S4).

For protein detection, ALP was selected as the analyte because ALP can catalyze the decomposition of phosphomonoesters such as AAP to produce the reduced product AA. Moreover, the commercially available ALP assay kit (using para-nitrophenyl phosphate as a chromogenic substrate) was used as a control to compare with ours. As shown in Figures S16g,h and S20a,b and Table S5, both two probes can detect ALP with high sensitivity at RT. The detection limits of the kit (0.078 U L^{-1}) and our probe (0.10 U L^{-1}) are relatively close (Figures S16i, S20c, and 4o). Then, we compared the ability of these two probes to detect ALP at 0 °C (Figures 4g−i and S20d,e and Table S5). The result exhibited that the effect of lower temperature caused the commercial kit's detection limit to increase by 7.8 times (Figure 4l,o). In contrast, our cold-adapted biosensor is more tolerant to temperature, with its detection limit changing less at 0 °C and being lower than that of the commercial kit, demonstrating its powerful low-temperature adaptive detection capability (Figure 4o).

Low-Temperature Adaptive Detection of Cellular GSH. To assess the performance of the cold-adaptive nanozyme probe in analyzing complex samples, we used it to detect GSH levels in cell lysates at RT and 0 °C. As a key antioxidant in organisms, abnormal intracellular GSH levels are often linked to various diseases.[41]

First, the probe was used to detect GSH at RT and 0 °C (Figure 5a). As shown in Figure S21a, the UV−visible characteristic absorption of TMB_{ox} gradually decreased as the GSH concentration increased from 0 to 60 μM at RT. Within the range of 1−10 μM, the characteristic absorbance of TMB_{ox} exhibited a linear relationship with the GSH concentration (R^2 = 0.99794) (Figure S21b). The detection limit of the probe at RT was approximately 0.25 μM (S = 3σ) (Figure 5i). Comparatively, at 0 °C, the probe also demonstrated excellent detection performance for GSH. Within the range of 1−20 μM, the absorbance of TMB_{ox} at 652 nm showed a good linear relationship with the GSH concentration (R^2 = 0.99106), with a detection limit of approximately 0.43 μM (Figure 5b,c,f,i). These results indicate that the decrease in temperature has minimal interference on this probe's ability to detect GSH.

Then, the cold-adaptive probe was further utilized to evaluate the GSH content in normal cells (L929) and cancer cells (4T1) at both RT and 0 °C (Figure 5d). As shown in the Figure S21c, at room temperature, the characteristic absorbance of TMB_{ox} gradually decreased as the cell density of L929 and 4T1 cells (cells/mL) increased from 4 × 10^4 to 25 × 10^4. This reduction is attributed to the effective inhibition of oxidase-like catalysis by intracellular GSH. Notably, the inhibitory effect observed in 4T1 cells was significantly greater than that in L929 cells, which aligns with the well-known phenomenon that GSH concentrations are higher in tumor cells compared to normal cells.[40,42] Meanwhile, we conducted the same tests at 0 °C, and the results indicated that the temperature reduction had a minimal impact on the evaluation of intracellular GSH levels in both cell types (Figure 5e,g,h,j,k). This demonstrates that the cold-adaptive nanozyme probe maintains good detection stability in complex samples even under low-temperature conditions.

Low-Temperature Adaptive Detection of Gas. Encouraging by such robust low-temperature adaptive detectability, we conducted further evaluations on gas samples using this probe. As shown in Figures 6a and S22a, we loaded this cold-adaptive nanozyme on filter paper to construct a paper-based colorimetric sensor and used it to detect H_2S gas (an important freshness indicator of meat). The production of H_2S gas mainly depends on two ways in this work: one is chemical reaction, that is, the reaction of Na_2S and HCl (Figure S22b); the other is natural meat spoilage at RT (Figure S22c). By observing the color changes on the paper with the naked eye and using a smartphone to take pictures and quantitatively analyze its RGB color, the results showed that our paper-based probe can successfully detect H_2S gas at both RT and 0 °C (Figure 6b−e). The probe has a low sensitivity for detecting

https://doi.org/10.1021/acssensors.4c02848
ACS Sens. 2025, 10, 1844−1856

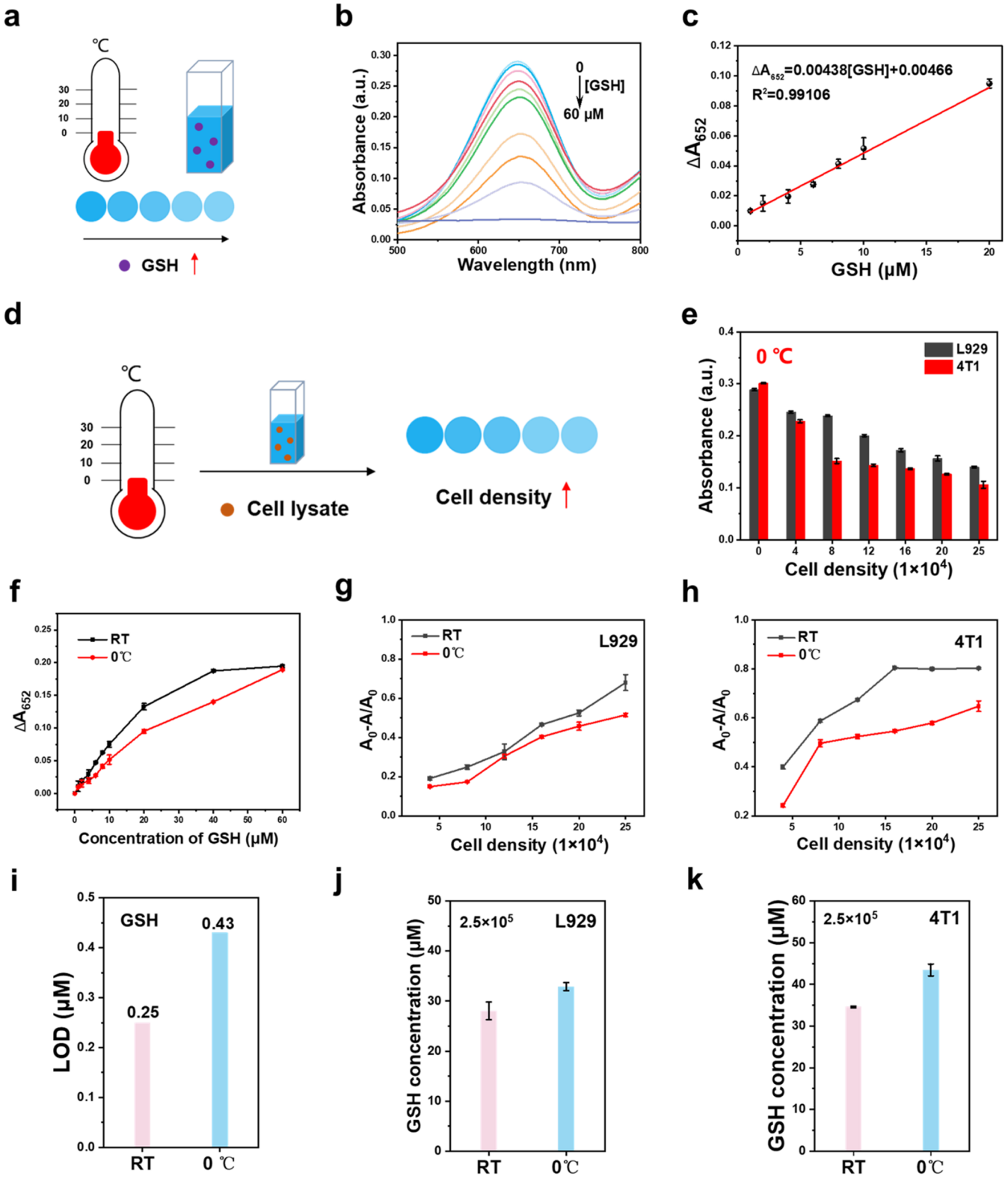

Figure 5. (a) Schematic diagram of the nanozyme probe detecting GSH at 0 °C. (b) UV−visible absorption spectra of samples containing TMB and $MnSn(OH)_{6-23-E10}$ in the absence and presence of GSH with different concentrations at 0 °C. (c) The linear calibration plotted in the concentration range from 1 to 20 μM at 0 °C. (d) Schematic diagram of the nanozyme probe detecting cell lysate at 0 °C. (e) Absorbance at 652 nm of TMB after catalytic oxidation with $MnSn(OH)_{6-23-E10}$ in the absence and presence of L929 and 4T1 cells at 0 °C. (f) Comparison of the sensitivity of nanozyme probes for GSH detection at RT and 0 °C. Comparison of the sensitivity of nanozyme probes for (g) L929 and (h) 4T1 cells detection at RT and 0 °C. (i) Detection limit of $MnSn(OH)_{6-23-E10}$ for GSH at RT and 0 °C. Qualitative evaluation of (j) L929 and (k) 4T1 cellular GSH levels with the developed sensor at RT and 0 °C. The number marked on the histogram is the cell density. Error bars in all figures mean standard deviations of 3 independent tests.

https://doi.org/10.1021/acssensors.4c02848
ACS Sens. 2025, 10, 1844−1856

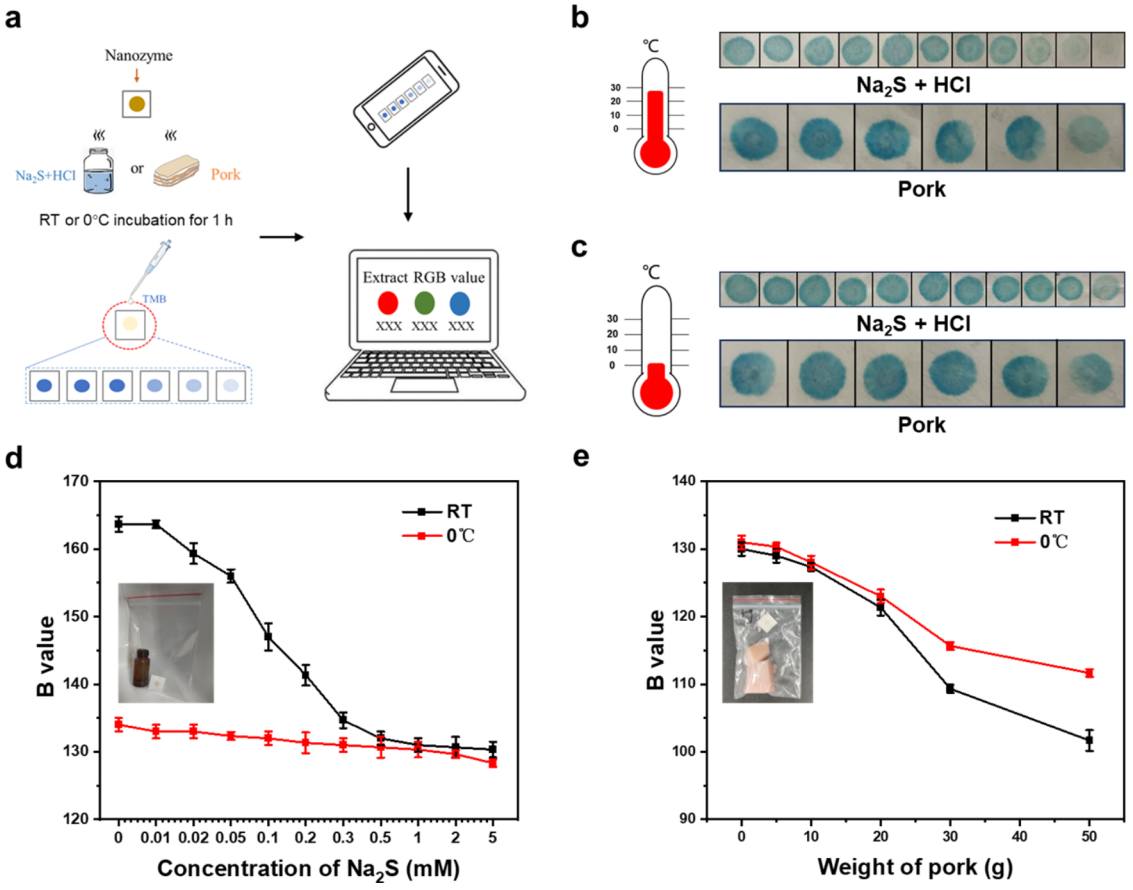

Figure 6. (a) Schematic diagram of nanozyme paper-based colorimetric sensor for detecting H_2S gas (detailed method can be found in the experiments). The nanozyme-based paper colorimetric sensor can detect H_2S gas produced during chemical reactions and meat spoilage, displaying obvious color changes at (b) RT and (c) 0 °C. (d) Plot of the B value of the nanozyme-based sensor versus the Na_2S concentration at RT and 0 °C. (e) Plot of B value of the nanozyme based sensor versus the weight of pork at RT and 0 °C. Error bars in all figures mean standard deviations of 3 independent tests.

H_2S gas at 0 °C, which may be because a low temperature inhibits the rates of the two reactions for generating H_2S gas, resulting in a lower H_2S concentration than at RT (Figure 6d,e).

CONCLUSIONS

In summary, we have constructed a new cold-adaptive nanozyme with excellent oxidase-like activity by modifying the perovskite hydroxide. The newly synthesized nanozyme increased its oxidase activity by 2 orders of magnitude and maintained more than 90% of its catalytic function at 0 °C. Through XPS, ICP-MS, and BET measurements, the increase in manganese content, vacancy oxygen, and tetravalent manganese may be the main reasons for the improvement of its activity. Then, we established a robust low-temperature adaptive biosensor using this nanozyme and systematically tested its detection capabilities for ions, small molecules, and proteins under RT and 0 °C. It is worth mentioning that the detection sensitivity of this probe for S^{2-}, AA, ALP, and cellular GSH at 0 °C was close to that at RT. Moreover, for the detection of ALP, this probe exhibited better sensitivity than a commercial ALP kit at 0 °C. Finally, using this nanozyme, we successfully constructed a paper-based gas probe and applied it to the detection of H_2S gas under RT and 0 °C. We hope that this research can offer novel insights and guidance for advancing the development and utilization of cold-adaptive nanozymes in the future.

ASSOCIATED CONTENT

Supporting Information

The Supporting Information is available free of charge at https://pubs.acs.org/doi/10.1021/acssensors.4c02848.

Figures S1−S23 and Tables S1−S6. XRD patterns, SEM images, ζ-potentials, XPS spectra, BET test results, kinetic assay, sensitivity detection results of S^{2-}, AA, ALP, and cell lysate at RT, selective detection results of S^{2-}, AA, and ALP at RT, fabrication process of paper-based H_2S gas sensor, comparison of this study with previous methods for detecting S^{2-}, AA, and ALP. (PDF)

AUTHOR INFORMATION

Corresponding Authors

Xuejiao J. Gao − *College of Chemistry and Materials, Jiangxi Normal University, Nanchang 330022, China;* orcid.org/0000-0001-7007-4417; Email: gaoxj@jxnu.edu.cn

Hui Wei − *Department of Biomedical Engineering, College of Engineering and Applied Sciences, Nanjing National Laboratory of Microstructures, Jiangsu Key Laboratory of Artificial Functional Materials, Nanjing University, Nanjing 210023 Jiangsu, China; State Key Laboratory of Analytical*

https://doi.org/10.1021/acssensors.4c02848
ACS Sens. 2025, 10, 1844−1856

Chemistry for Life Science, School of Chemistry and Chemical Engineering, Chemistry and Biomedicine Innovation Center (ChemBIC), Nanjing University, Nanjing 210023 Jiangsu, China; orcid.org/0000-0003-0870-7142; Email: weihui@nju.edu.cn

Dongzhi Yang − *Jiangsu Key Laboratory of New Drug Research and Clinical Pharmacy, Xuzhou Medical University, Xuzhou 221002 Jiangsu, China;* orcid.org/0000-0001-6796-1613; Email: dongzhiy@xzhmu.edu.cn

Authors

Yufeng Liu − *Jiangsu Key Laboratory of New Drug Research and Clinical Pharmacy, Xuzhou Medical University, Xuzhou 221002 Jiangsu, China;* orcid.org/0000-0002-2355-4706

Jing Zhang − *Jiangsu Key Laboratory of New Drug Research and Clinical Pharmacy, Xuzhou Medical University, Xuzhou 221002 Jiangsu, China*

Yuxin Wan − *College of Chemistry and Materials, Jiangxi Normal University, Nanchang 330022, China*

Cong Li − *Jiangsu Key Laboratory of New Drug Research and Clinical Pharmacy, Xuzhou Medical University, Xuzhou 221002 Jiangsu, China*

Shuai Cui − *Department of Pharmacy, The Second Affiliated Hospital of Xuzhou Medical University, General Hospital of Xuzhou Mining Group, Xuzhou 221006 Jiangsu, China*

Complete contact information is available at: https://pubs.acs.org/10.1021/acssensors.4c02848

Author Contributions

#Y.L., J.Z., and Y.W. contributed equally. The manuscript was written through contributions of all authors. All authors have given approval to the final version of the manuscript.

Funding

This work was supported by the National Key Research and Development Program of China (2024YFF1206803), National Natural Science Foundation of China (22307110, 22467013), the Natural Science Research General Project of Jiangsu Province Colleges and Universities (23KJD150009), Xuzhou Medical University Scientific Research Funding (D2022057), Gan Poyang talents support program, academic and technical leaders of major disciplines (20232BCJ23014).

Notes

The authors declare no competing financial interest.

REFERENCES

(1) Chan, Y. J.; Anwar, N.; Reuel, N. F. Cold and ultra-cold chain integrity monitoring via embedded resonant sensor indicators. *Sens. Actuators, A* **2024**, *372*, No. 115346.

(2) Badia-Melis, R.; Mc Carthy, U.; Ruiz-Garcia, L.; Garcia-Hierro, J.; Villalba, J. R. New trends in cold chain monitoring applications-A review. *Food Control* **2018**, *86*, 170−182.

(3) Gill, P.; Ghaemi, A. Nucleic acid isothermal amplification technologies—a review. *Nucleosides, Nucleotides Nucleic Acids* **2008**, *27*, 224−243.

(4) Zhao, Y.; Chen, F.; Li, Q.; Wang, L.; Fan, C. Isothermal amplification of nucleic acids. *Chem. Rev.* **2015**, *115*, 12491−12545.

(5) Saiki, R. K.; Gelfand, D. H.; Stoffel, S.; Scharf, S. J.; Higuchi, R.; Horn, G. T.; Mullis, K. B.; Erlich, H. A. Primer-directed enzymatic amplification of DNA with a thermostable DNA polymerase. *Science* **1988**, *239*, 487−491.

(6) Scrimin, P.; Prins, L. J. Sensing through signal amplification. *Chem. Soc. Rev.* **2011**, *40*, 4488−4505.

(7) Petersen, H. A.; Miller, E. N.; Pham, P. H.; Kajal; Katsirubas, J. L.; Koltunski, H. J.; Luca, O. R. On the Temperature Sensitivity of Electrochemical Reaction Thermodynamics. *ACS Phys. Chem. Au* **2023**, *3*, 241−251.

(8) Flatscher, M.; Neumayer, M.; Bretterklieber, T. Maintaining critical infrastructure under cold climate conditions: A versatile sensing and heating concept. *Sens. Actuators, A* **2017**, *267*, 538−546.

(9) Bowers, L. D.; Carr, P. W. Applications of immobilized enzymes in analytical chemistry. *Anal. Chem.* **1976**, *48*, 544A−559A.

(10) Guilbault, G. G. *Analytical Uses of Immobilized Enzymes*; M. Dekker, 1984; Vol. *2*.

(11) Low, P. S.; Bada, J. L.; Somero, G. N. Temperature adaptation of enzymes: roles of the free energy, the enthalpy, and the entropy of activation. *Proc. Natl. Acad. Sci. U.S.A.* **1973**, *70*, 430−432.

(12) Somero, G. N. Proteins and temperature. *Annu. Rev. Physiol.* **1995**, *57*, 43−68.

(13) Arcus, V. L.; Van Der Kamp, M. W.; Pudney, C. R.; Mulholland, A. J. Enzyme evolution and the temperature dependence of enzyme catalysis. *Curr. Opin. Struct. Biol.* **2020**, *65*, 96−101.

(14) Kuah, E.; Toh, S.; Yee, J.; Ma, Q.; Gao, Z. Enzyme mimics: advances and applications. *Chem. − Eur. J.* **2016**, *22*, 8404−8430.

(15) Murakami, Y.; Kikuchi, J.-i.; Hisaeda, Y.; Hayashida, O. Artificial enzymes. *Chem. Rev.* **1996**, *96*, 721−758.

(16) Lin, Y.; Ren, J.; Qu, X. Catalytically active nanomaterials: a promising candidate for artificial enzymes. *Acc. Chem. Res.* **2014**, *47*, 1097−1105.

(17) Liang, M.; Yan, X. Nanozymes: From New Concepts, Mechanisms, and Standards to Applications. *Acc. Chem. Res.* **2019**, *52*, 2190−2200.

(18) Gao, L.; Zhuang, J.; Nie, L.; Zhang, J.; Zhang, Y.; Gu, N.; Wang, T.; Feng, J.; Yang, D.; Perrett, S.; Yan, X. Intrinsic peroxidase-like activity of ferromagnetic nanoparticles. *Nat. Nanotechnol.* **2007**, *2*, 577−583.

(19) Cai, X.; Huang, Y.; Zhu, C. Immobilized Multi-Enzyme/Nanozyme Biomimetic Cascade Catalysis for Biosensing Applications. *Adv. Healthcare Mater.* **2024**, No. 2401834.

(20) Zhuang, J.; Midgley, A. C.; Wei, Y.; Liu, Q.; Kong, D.; Huang, X. Machine-Learning-Assisted Nanozyme Design: Lessons from Materials and Engineered Enzymes. *Adv. Mater.* **2024**, *36*, No. 2210848.

(21) Robert, A.; Meunier, B. How to Define a Nanozyme. *ACS Nano* **2022**, *16*, 6956−6959.

(22) Wang, Q.; Wei, H.; Zhang, Z.; Wang, E.; Dong, S. Nanozyme: An emerging alternative to natural enzyme for biosensing and immunoassay. *TrAC, Trends Anal. Chem.* **2018**, *105*, 218−224.

(23) Zandieh, M.; Liu, J. Nanozyme Catalytic Turnover and Self-Limited Reactions. *ACS Nano* **2021**, *15*, 15645−15655.

(24) Zhang, R.; Jiang, B.; Fan, K.; Gao, L.; Yan, X. Designing nanozymes for in vivo applications. *Nat. Rev. Bioeng.* **2024**, *2*, 849−868.

(25) Wu, J.; Wang, X.; Wang, Q.; Lou, Z.; Li, S.; Zhu, Y.; Qin, L.; Wei, H. Nanomaterials with enzyme-like characteristics (nanozymes): next-generation artificial enzymes (II). *Chem. Soc. Rev.* **2019**, *48*, 1004−1076.

(26) Zhang, Y.; Wei, G.; Liu, W.; Li, T.; Wang, Y.; Zhou, M.; Liu, Y.; Wang, X.; Wei, H. Nanozymes for nanohealthcare. *Nat. Rev. Methods Primers* **2024**, *4*, 36.

(27) Tian, Q.; Li, S.; Tang, Z.; Zhang, Z.; Du, D.; Zhang, X.; Niu, X.; Lin, Y. Nanozyme-Enabled Biomedical Diagnosis: Advances, Trends, and Challenges. *Adv. Healthcare Mater.* **2024**, No. 2401630.

(28) Chen, Y.; Tian, Q.; Wang, H.; Ma, R.; Han, R.; Wang, Y.; Ge, H.; Ren, Y.; Yang, R.; Yang, H. A Manganese-Based Metal−Organic Framework as a Cold-Adapted Nanozyme. *Adv. Mater.* **2024**, *36*, No. 2206421.

(29) Ameen, S. S. M.; Omer, K. M. Temperature-resilient and sustainable Mn-MOF oxidase-like nanozyme (UoZ-4) for total antioxidant capacity sensing in some citrus fruits: Breaking the temperature barrier. *Food Chem.* **2024**, *448*, No. 139170.

(30) Qin, T.; Chen, Y.; Miao, X.; Shao, M.; Xu, N.; Mou, C.; Chen, Z.; Yin, Y.; Chen, S.; Yin, Y.; et al. Low-Temperature Adaptive Single-Atom Iron Nanozymes against Viruses in the Cold Chain. *Adv. Mater.* **2024**, *36*, No. 2309669.
(31) Gai, P.; Pu, L.; Wang, C.; Zhu, D.; Li, F. CeO_2@NC nanozyme with robust dephosphorylation ability of phosphotriester: a simple colorimetric assay for rapid and selective detection of paraoxon. *Biosens. Bioelectron.* **2023**, *220*, No. 114841.
(32) Zou, Y.; Jin, B.; Li, H.; Wu, X.; Liu, Y.; Zhao, H.; Zhong, D.; Wang, L.; Chen, W.; Wen, M.; Liu, Y. N. Cold nanozyme for precise enzymatic antitumor immunity. *ACS Nano* **2022**, *16*, 21491−21504.
(33) Gao, Y.; Ye, L.; Cao, S.; Chen, H.; Yao, Y.; Jiang, J.; Sun, L. Perovskite hydroxide $CoSn(OH)_6$ nanocubes for efficient photo-reduction of CO_2 to CO. *ACS Sustainable Chem. Eng.* **2018**, *6*, 781−786.
(34) Song, F.; Schenk, K.; Hu, X. A nanoporous oxygen evolution catalyst synthesized by selective electrochemical etching of perovskite hydroxide CoSn(OH)6 nanocubes. *Energy Environ. Sci.* **2016**, *9*, 473−477.
(35) Liu, Y.; Cheng, Y.; Zhang, H.; Zhou, M.; Yu, Y.; Lin, S.; Jiang, B.; Zhao, X.; Miao, L.; Wei, C.-W.; et al. Integrated cascade nanozyme catalyzes in vivo ROS scavenging for anti-inflammatory therapy. *Sci. Adv.* **2020**, *6*, No. eabb2695.
(36) Zhang, X.; Wang, Z.; Huang, X.; Huang, Q.; Wen, Y.; Li, B.; Holmes, M.; Shi, J.; Zou, X. Uniform stain pattern of robust MOF-mediated probe for flexible paper-based colorimetric sensing toward environmental pesticide exposure. *Chem. Eng. J.* **2023**, *451*, No. 138928.
(37) Zhai, X.; Li, Z.; Shi, J.; Huang, X.; Sun, Z.; Zhang, D.; Zou, X.; Sun, Y.; Zhang, J.; Holmes, M.; et al. A colorimetric hydrogen sulfide sensor based on gellan gum-silver nanoparticles bionanocomposite for monitoring of meat spoilage in intelligent packaging. *Food Chem.* **2019**, *290*, 135−143.
(38) Liu, Y.; Zhang, J.; Cui, S.; Wei, H.; Yang, D. Perovskite hydroxide-based laccase mimics with controllable activity for environmental remediation and biosensing. *Biosens. Bioelectron.* **2024**, *256*, No. 116275.
(39) Wu, H.; Lu, Q.; Li, Y.; Zhao, M.; Wang, J.; Li, Y.; Zhang, J.; Zheng, X.; Han, X.; Zhao, N.; et al. Structural framework-guided universal design of high-entropy compounds for efficient energy catalysis. *J. Am. Chem. Soc.* **2023**, *145*, 1924−1935.
(40) Liu, Y.; Zhou, M.; Cao, W.; Wang, X.; Wang, Q.; Li, S.; Wei, H. Light-responsive metal−organic framework as an oxidase mimic for cellular glutathione detection. *Anal. Chem.* **2019**, *91*, 8170−8175.
(41) Smeyne, M.; Smeyne, R. J. Glutathione metabolism and Parkinson's disease. *Free Radical Biol. Med.* **2013**, *62*, 13−25.
(42) Wei, C.; Liu, X.; Gao, Y.; Wu, Y.; Guo, X.; Ying, Y.; Wen, Y.; Yang, H. Thiol−disulfide exchange reaction for cellular glutathione detection with surface-enhanced Raman scattering. *Anal. Chem.* **2018**, *90*, 11333−11339.

https://doi.org/10.1021/acssensors.4c02848
ACS Sens. 2025, 10, 1844−1856